

ORBITAL MIGRATION OF INTERACTING LOW-MASS PLANETS IN EVOLUTIONARY RADIATIVE TURBULENT MODELS

BRANDON HORN¹, WLADIMIR LYRA^{2,3,4},
MORDECAI-MARK MAC LOW^{1,2,5},
AND
ZSOLT SÁNDOR^{5,6}
Draft version March 29, 2021

ABSTRACT

The torques exerted by a locally isothermal disk on an embedded planet lead to rapid inward migration. Recent work has shown that modeling the thermodynamics without the assumption of local isothermality reveals regions where the net torque on an embedded planet is positive, leading to outward migration of the planet. When a region with negative torque lies directly exterior to this, planets in the inner region migrate outwards and planets in the outer region migrate inwards, converging where the torque is zero. We incorporate the torques from an evolving non-isothermal disk into an N -body simulation to examine the behavior of planets or planetary embryos interacting in the convergence zone. We find that mutual interactions do not eject objects from the convergence zone. Small numbers of objects in a laminar disk settle into near resonant orbits that remain stable over the 10 Myr periods that we examine. However, either or both increasing the number of planets or including a correlated, stochastic force to represent turbulence drives orbit crossings and mergers in the convergence zone. These processes can build gas giant cores with masses of order ten Earth masses from sub-Earth mass embryos in 2–3 Myr.

1. INTRODUCTION

The details of how giant planets form in protoplanetary disks remain poorly understood. The core accretion model developed by Pollack et al. (1996) relies on the rapid growth of a gas giant through runaway accretion of gas onto a solid planetary core that grows massive enough to gravitationally capture the gas. Such cores form through binary collisions of planetary embryos—the bodies formed during oligarchic growth, with masses ranging from $0.1 M_{\oplus}$ to a few Earth masses. Since the accretion must necessarily occur in a gas-rich disk, the planetary core must be formed before the gas disk dissipates. The mass required to begin rapidly accreting gas is determined by the aspect ratio of the disk, the mass of the star, and the luminosity of the core that is provided by planetesimal accretion and can prevent collapse of the accreting gas. For a solar mass star, a thin disk with an aspect ratio of 0.05, and a surface density of planetesimals of 10 g cm^{-2} at 5 AU, the core must be around ten Earth masses to begin runaway accretion. The lifetime of the gas disk is on the order of 10 Myr, and the core must form before the disk dissipates.

Planetary embryos are massive enough to not be affected by the gas drag forces that dominate the motion

of smaller bodies moving through the sub-Keplerian gas disk. The mass of the planetary embryos, however, induces spiral Lindblad resonances in the gas disk. The asymmetry in the size of the inner and outer Lindblad resonances generates a net negative torque from the disk that, in the absence of other effects, robs the planet of angular momentum, leading to inward Type I migration and ultimately infall into the central star. A linear treatment of the torque from isothermal gas in the co-rotating region of the planetary embryo shows that it provides a positive torque arising from the presence of a vortensity gradient that nearly offsets the net Lindblad torque, but a small net negative torque remains.

The behavior of multiple planetary embryos embedded in a gas disk and undergoing inward migration due to Lindblad and linear co-rotational torques was explored by Cresswell & Nelson (2008). They found that as bodies with different masses migrate inwards, differential migration leads to mergers, forming bodies with masses in the planetary core range. These simulations use large embryos—with masses of at least $2 M_{\oplus}$ and up to planetary core mass—and simulate migration in a laminar, isothermal disk.

In addition to the perturbations to the gas disk caused by the presence of the planetary embryos, a partially ionized disk with a subthermal magnetic field can develop turbulence through the magnetorotational instability (MRI, Balbus & Hawley 1991). The resulting random overdensities in the gas can lead the planetary embryo to undergo a random walk, possibly avoiding infall for some of the bodies (Nelson 2005). While this is an effective way to prevent catastrophic infall for planetesimal-sized objects with radii of $< 1000 \text{ km}$ (Yang et al. 2009, 2011), it does not provide a clear mechanism for building large planetary cores.

Planetary embryos undergoing inward Type I migration can be trapped in pressure ridges that may form in the presence of a dead-zone boundary or within an anti-

¹ Department of Astronomy, Columbia University, 550 West 120th St, New York, NY 10027, USA; bhorn@astro.columbia.edu

² Department of Astrophysics, American Museum of Natural History, 79th Street at Central Park West, New York, NY 10024, USA; wlyra@amnh.org, mordecai@amnh.org

³ Jet Propulsion Laboratory, 4800 Oak Grove Drive, Pasadena, CA 91109, USA

⁴ NASA Carl Sagan Fellow

⁵ Max-Planck-Institut für Astronomie, Königstuhl 17, 69117, Heidelberg, Germany

⁶ Institut für Astro und Teilchenphysik, Leopold Franzens Universität Innsbruck, Technikerstrasse 25/8, A-6020 Innsbruck, Austria; zsolt.sandor@uibk.ac.at

cyclonic vortex. The positive gradient in surface density in these regions leads to formation of a convergence zone, where migration halts. The dynamics of multiple planetary embryos undergoing Type I migration in the proximity of a pressure ridge convergence zone have been investigated by Morbidelli et al. (2008), who found that planets collide until only a few remain. Sándor et al. (2011) showed that such pressure traps can lead to growth from planetary embryos to planetary cores through continual generation of bodies that migrate into the pressure ridge convergence zone.

One possible means of avoiding catastrophic infall that could lead to rapid formation of planetary cores was found by Paardekooper & Mellema (2006), who explored the interactions of planets with a gas disk, in a model in which they did not make the locally isothermal approximation, but rather directly modeled the effects of radiative transfer through optically thick gas with an adiabatic equation of state. They found that the co-rotation torque arising from the gas undergoing horseshoe turns near the planet showed a strong positive contribution when the isothermal approximation was relaxed. This was later shown to be a result of the presence of an entropy gradient across the corotation region (Paardekooper & Papaloizou 2008; Baruteau & Masset 2008). A large radial entropy gradient increases the positive co-rotation torque to the point that it cancels out the negative net Lindblad torque and can even reverse the direction of migration. This understanding was developed further in Paardekooper & Papaloizou (2009). A prescription for the nonlinear horseshoe torque was given by Paardekooper et al. (2010), allowing the total torque on a planet undergoing Type I migration to be calculated, given the local temperature and surface density gradients. The migration of a single planet embedded in an evolving disk was then studied by Lyra et al. (2010, hereafter LPM10), who found that planets migrate towards convergence zones, where the net torque is zero. Planets located exterior to these orbits experience a negative torque, while planets located interior experience a positive torque. Upon reaching the zero-torque region, the planets migrate inwards with the disk until the disk dissipates, thus avoiding collision with the star.

In this paper, we extend the work of LPM10 by following the interactions of multiple planets converging towards any zero-torque radius. We use the disk evolution model from LPM10, for a non-isothermal one-dimensional disk with photoevaporation and viscous diffusion. The radial profiles of temperature and surface density from the disk evolution model are used to determine the torque on planetary embryos in an N -body simulation, following the formula for non-isothermal, unsaturated, horseshoe torque of Paardekooper et al. (2010). An optimized version of the Bulirsch-Stoer N -body code used in Sándor et al. (2011) is employed to integrate the orbits of the planets under the influence of the torque from the gas disk, as well as eccentricity and inclination damping following Cresswell & Nelson (2008). The code was modified to include the effect of turbulence on the planetary motion, using the prescription described by Laughlin et al. (1994).

We start in Sect. 2 by describing the disk model, the prescriptions for the torque, eccentricity and inclination

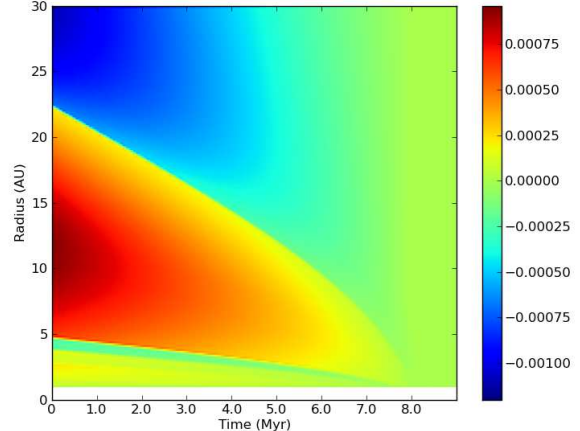


FIG. 1.— The dimensionless migration torque and how it evolves through time. The region of interest in these simulations is the transition from negative torque - inward migration - to positive torque that is initially located around 22 AU. As the disk evolves, this convergence zone moves inwards. The torque shown in this figure is an interpolation between the adiabatic and isothermal torques, based on the opacity at a given radius. To find the torque acting on a body at a given location, this dimensionless torque must be multiplied by Γ_0 , from Eq. (12).

damping, the turbulence model, and how they are included in the N -body code. In Sect. 3, we describe the initial conditions of the planets in the simulations as well as the parameters describing the different gas disks that were used. Section 4 presents the results of the simulations and Sect. 5 includes a discussion of the results. A study tackling a similar problem was made public after initial submission of our paper by Hellary & Nelson (2012, hereafter HN12). We discuss the differences between our work and theirs in Sect. 5.1. A summary and conclusions are presented in Sect. 6.

2. METHOD

Our simulation can be viewed as a modified N -body simulation, which incorporates the migration torques acting on planetary embryos, a stochastic force representing turbulence in the gas disk, and eccentricity and inclination damping from the gas disk, as well as the disk evolution due to viscosity and photoevaporation. The migration torques depend on temperature and surface density profiles from one-dimensional simulations of the evolution of the gas disk, and the force from turbulence is modeled using a time-dependent potential. Each component of the simulation is described in more detail in this section.

2.1. Disk Evolution

The gas disk evolves via viscous diffusion and photoevaporation. The evolution of the gas surface density due to viscosity is given by (Lynden-Bell & Pringle 1974)

$$\frac{\partial \Sigma}{\partial t} = \frac{3}{r} \frac{\partial}{\partial r} \left[r^{1/2} \frac{\partial \Sigma \nu r^{1/2}}{\partial r} \right], \quad (1)$$

where r is the distance from the central star, and ν is the kinematic viscosity. Following Shakura & Sunyaev

TABLE 1
RUN PARAMETERS

Run (1)	M_p (2)	μ_{mass} (3)	σ_{mass} (4)	Combine (5)	N_p (6)	N_{mHR} (7)	M_{tot} (8)	Swarm (9)	T_{form} (10)	M_{core} (11)
H1 (Fiducial)	0.75	–	–	–	23	3	17.25	No	1.29	10.5
H2	0.5	–	–	–	27	3	13.5	No	2.23	8.0
H3	1.00	–	–	–	21	3	21.0	No	0.43	13.0
H4	1.25	–	–	–	20	3	25.0	No	0.21	10.0
H5	1.5	–	–	–	19	3	29.5	No	0.15	10.5
G1	–	1.0	0.3	–	21	3	20.9	No	0.27	11.1
G2	–	1.0	0.3	–	11	6	11.7	No	0.34	7.1
G3	–	0.75	0.3	–	24	3	18.7	No	2.38	10.2
G4	–	0.75	0.3	–	13	6	9.8	No	1.49	9.3
G5	–	0.5	0.2	–	27	3	13.9	No	3.18	9.3
G6	–	0.5	0.2	–	14	6	6.2	No	1.38	4.4
G7	–	–	–	G2+G6	25	6	17.9	No	1.36	12.0
G8	–	–	–	G2+G4	24	6	21.5	No	0.95	10.5
G9	–	–	–	G4+G6	27	6	16.0	No	2.64	9.4
Sw1	0.25	–	–	–	25	4	6.25	Yes	4.60	2.5
Sw2	0.75	–	–	–	12	6	9	Yes	4.41	8.5
Sw3	1.0	–	–	–	11	6	11	Yes	0.68	8.5
Sw4	1.0	–	–	–	7	10	7	Yes	1.42	9.0
SD1	0.75	–	–	–	23	–	17.25	No	0.98	10.5
SD2	1.0	–	–	–	17	–	17.0	No	0.267	7.0 & 5.0
SD3	–	0.75	0.3	–	21	–	17.26	No	1.03	10.2

NOTE. — Col. (1): Name of run. Col. (2): Initial mass of bodies, in M_{\oplus} . Col. (3): Mean of Gaussian distribution for initial masses, in M_{\oplus} . Col. (4): Standard deviation of Gaussian distribution for initial masses, in M_{\oplus} . Col. (5): Combined initial sample. Col. (6): Number of initial planets. Col. (7): Initial separation between planets, in mutual Hill radii. Col. (8): Total initial mass. Col. (9): Presence of background swarm of small ($0.25 M_{\oplus}$) planets. Col. (10): Formation time (Myr). Col. (11): Mass of the core formed, in M_{\oplus} .

(1973) we use

$$v = \alpha c_s^2 / \Omega \quad (2)$$

where α is a dimensionless parameter. The Keplerian angular velocity is

$$\Omega = (GM_{\star}/r^3)^{1/2}, \quad (3)$$

where M_{\star} is the mass of the central star, and c_s is the local sound speed. Our simulation uses a model based on the results of Hollenbach et al. (1994) to specify the rate of surface density loss due to photoevaporation. This occurs only beyond a radius r_g where ionized disk gas has a sound speed equal to the escape velocity. In this regime

$$\dot{\Sigma}_w = \frac{\dot{M}_w r_g^{1.5}}{2\pi (r_{\text{ext}} - r_g) r^{2.5}}, \quad (4)$$

while $\dot{\Sigma}_w = 0$ within. The rate of photoevaporation is set by the wind mass loss rate \dot{M}_w , the escape radius r_g , and the external boundary of our simulation r_{ext} . As the gas disk evolves, we record temperature and surface density profiles every 10^3 yr.

For temperature evolution, we use a model without shock heating (Nakamoto & Nakagawa 1994) that balances viscous heating, background radiation, and radiative cooling to derive an emerging flux

$$2\sigma T^4 = \tau_{\text{eff}} \left(\frac{9}{4} \Sigma v \Omega^2 \right) + 2\sigma T_b^4, \quad (5)$$

where T and T_b are the midplane and background temperatures, and σ the Stefan-Boltzmann constant. We take the effective optical depth at the midplane (Hubeny

1990; Kley & Crida 2008)

$$\tau_{\text{eff}} = \frac{3\tau}{8} + \frac{\sqrt{3}}{4} + \frac{1}{4\tau}. \quad (6)$$

The optical depth is $\tau = \kappa \Sigma / 2$, and the opacities κ are taken from Bell et al. (1997). We assume that although dust growth and planet formation lock away refractory material, fragmentation efficiently replenishes small grains, keeping the disks opaque during their evolution (Birnstiel et al. 2009).

The gas simulations are conducted using the same numerical algorithm as LPM10, which evolves the gas disk in one dimension over the lifetime of the disk. As a numerical solver, we used the PENCIL CODE⁷, which integrates the equations of evolution with sixth order spatial derivatives, and a third order Runge-Kutta time integrator. Boundary conditions are taken as outflow. Because the optical depth depends on temperature, we solve Eq. (5) with a Newton-Raphson root-finding algorithm (using 0.01 K precision). To save on computational time, temperatures are pre-computed as a function of Σ and Ω , stored in the memory as look-up tables, and retrieved in run time via bilinear interpolation.

The reduction to one dimension assumes azimuthal symmetry and that the disk can be vertically integrated without significantly changing the characteristics of the disk. The azimuthal asymmetry will be reintroduced into the simulation via our migration and turbulence prescriptions, and the scale-height parameterizes the effects of a finite disk height on the magnitude of the turbulence as well as setting the timescales for eccentricity and inclination damping.

⁷ The code, including improvements done for the present work, is publicly available under a GNU open source license and can be downloaded at <http://www.nordita.org/software/pencil-code>

The profiles from the gas simulations are used to determine the local temperature and gas surface density in the N -body code. The migration torques and turbulent forces acting on the planets are proportional to the local surface density Σ and temperature T . The local values of Σ and T at any given time and position are found by linearly interpolating from the two closest times, and then again between the two nearest radial grid points.

Several quantities are indirectly dependent on T by way of the local sound speed,

$$c_s = \sqrt{\frac{\gamma kT}{\mu m_H}}, \quad (7)$$

where γ is the adiabatic coefficient of the gas, set to 7/5 for diatomic molecules, k is Boltzmann's constant, μ is the mean molecular weight of the gas, set to 2.4 for a 5:1 H₂-He mixture, and m_H is the mass of a hydrogen atom. The sound speed is also used to determine the aspect ratio of the disk

$$h = \frac{H}{r} = \frac{c_s}{v_K} \quad (8)$$

where H is the scale height of the disk, and the Keplerian velocity $v_K = (GM_*/r)^{1/2}$. Unless otherwise noted, Σ , c_s , H and h are time and radius dependent, with values derived from the gas evolution model.

The local radial gradients of temperature and surface density needed for the torque calculation are calculated for the entire disk during its evolution using a sixth-order, finite-difference method, as is done in the PENCIL CODE. The gradients are recorded with the density and temperature profiles. During the N -body simulation, the same linear interpolation method is used for the gradients as for the original quantities.

We ignore gap opening by massive planets, since that does not occur for planets with masses less than 10–20 M_\oplus (Crida et al. 2006), and the goal of this simulation is to examine whether planetary embryos can coalesce into planets with masses approaching this regime. Therefore, we can simplify the simulations by evolving the gas disk for its entire lifetime before beginning the N -body simulations.

2.2. Prescription for migration

Planets in a gas disk induce spiral Lindblad resonances in the disk, as well as driving the gas in the co-orbital region into horseshoe orbits. The net torque on the planet from the Lindblad resonances can be calculated analytically, as in Ward (1997). In isothermal, non-magnetized disks, the full net torque (Lindblad and co-rotational) can be calculated semi-analytically (Tanaka & Ward 2004). The Lindblad resonances impart a negative torque to the planet, leading to the well known effect of rapid inward migration. Hydrodynamical simulations of a planet with mass on the order of M_\oplus embedded in an isothermal disk have confirmed the predictions from linear theory (Bate et al. 2003; D'Angelo et al. 2002).

Paardekooper & Mellema (2006) investigated the migration of a low-mass planet in an adiabatic, hydrodynamic simulation including radiative transfer for cooling radiation, and showed that outward migration can occur in such a non-isothermal disk due to positive

torques exerted by the co-rotation region under some circumstances. Later investigations showed that this departure from isothermal Type I migration is caused by the radial entropy gradient of the disk (Paardekooper & Papaloizou 2008; Baruteau & Masset 2008). A prescription incorporating the effects of non-isothermal co-rotation torques was developed by Paardekooper et al. (2010).

The prescription allows us to calculate the torque acting on a low-mass planet embedded in a gas disk as a function of the radial gradient of the disk's temperature and density in the region near the planet. Defining the gradients as

$$\eta = \frac{\partial \ln \Sigma}{\partial \ln r}; \quad \beta = \frac{\partial \ln T}{\partial \ln r}; \quad \zeta = \beta - (\gamma - 1)\eta, \quad (9)$$

Paardekooper et al. (2010) arrived at the following equation for the total unsaturated torque on the planet

$$\gamma \Gamma_{\text{ad}} / \Gamma_0 = -0.85 - \eta - 1.75\beta + 7.9\zeta / \gamma. \quad (10)$$

If the gas passing through the horseshoe turn cools rapidly enough, the co-rotational torque is best approximated by the isothermal model

$$\Gamma_{\text{iso}} / \Gamma_0 = -0.85 - \eta - 0.9\beta. \quad (11)$$

The scale of both torques is set by

$$\Gamma_0 = \left(\frac{q}{h}\right)^2 \Sigma r^4 \Omega^2, \quad (12)$$

where q is the ratio of the planet mass to the central stellar mass, is the distance from the planet to the central body. This prescription is valid for low mass planets in unsaturated regions.

If the gas can radiate away the surplus heat and restore the temperature quickly, then the gas exerting the horseshoe drag should be treated isothermally. The effective torque is interpolated between the isothermal and adiabatic torque models. The ratio of the radiative cooling time, t_{rad} , to the dynamical time, t_{dyn} , defines the interpolation between the two regimes. We estimate

$$t_{\text{rad}} \sim E / \dot{E}, \quad (13)$$

where \dot{E} is the rate of cooling by radiation, or equivalently the divergence of the radiation flux, F , and E is the internal energy density of the gas, $E = c_V \rho T$. For a cylinder of height $2H$ centered on the disk, $\rho = \Sigma / 2H$, and the total energy within the cylinder is

$$\int E dV = \int \frac{c_V \Sigma T}{2H} dV = \pi r^2 c_V \Sigma T, \quad (14)$$

where the last step is true for a cylinder with a small radius with constant temperature and surface density throughout. Integrating the rate of cooling over the same volume gives

$$\int \dot{E} dV = \int \nabla \cdot F dV = \oint F dS = 2\pi r^2 \sigma T_{\text{eff}}^4. \quad (15)$$

This is true for small radii if the temperature outside of the cylinder is nearly the same as the temperature inside, since then the flux is approximately zero every-

where except the top and bottom of the cylinder. Substituting $T_{\text{eff}}^4 = T^4 / \tau_{\text{eff}}$, the radiation timescale is

$$\frac{E}{\dot{E}} = \frac{c_V \Sigma \tau_{\text{eff}}}{2\sigma T^3}. \quad (16)$$

Defining Θ to be the ratio of the radiative timescale to the dynamic timescale $2\pi / \Omega$, we have

$$\Theta = \frac{c_V \Sigma \Omega \tau_{\text{eff}}}{4\pi \sigma T^3}. \quad (17)$$

The effective torque acting on a planet is then given by interpolating between the adiabatic and isothermal torques

$$\Gamma_{\text{typeI}} = \frac{\Gamma_{\text{ad}} \Theta^2 + \Gamma_{\text{iso}}}{(\Theta + 1)^2}. \quad (18)$$

This interpolation, though not derived from physical principles, provides a smooth mathematical transition between the isothermal and adiabatic limits. We stress, though, that the precise nature of the transition has little influence on the results since, as shown in LPM10, most of the planet evolution in the disk through space and time occurs well within the adiabatic regime. The resulting torques are shown in Fig. 1.

2.3. Prescription for eccentricity and inclination damping

In addition to the torque that is responsible for Type I migration, the gas disk also imparts a force on a planet that acts to dampen the planet's eccentricity e and inclination i (Tanaka & Ward 2004). This dampening can be modeled as an exponential decay. Tanaka and Ward (2004) provide the timescale

$$t_{\text{damp}} = \frac{M_*^2 h^4}{m_p \Sigma a_p^2 \Omega} \quad (19)$$

where a_p is the semi-major axis of the planet, and the disk aspect ratio h is given by equation (8). Cresswell & Nelson (2008) showed that the exponential decay is only applicable for small inclinations and eccentricities, after which point the decay is best modeled as a power law. Following their prescriptions, we use the following timescales for the dampening of eccentricity and inclination, respectively

$$t_e = \frac{t_{\text{damp}}}{0.780} \left(1 - 0.14\varepsilon^2 + 0.06\varepsilon^3 + 0.18\varepsilon l^2 \right) \quad (20)$$

$$t_i = \frac{t_{\text{damp}}}{0.544} \left(1 - 0.30l^2 + 0.24l^3 + 0.14l\varepsilon^2 \right) \quad (21)$$

where $\varepsilon = e/h$ and $l = i/h$.

These equations give a timescale for the damping that agrees well with hydrodynamic simulations over the range of eccentricities and inclinations observed in our simulations⁸. The timescales are calculated at each step

⁸ These timescales were derived for isothermal disks. However, Bitsch & Kley (2010, 2011) show that the behavior in radiative disks is qualitatively similar. The quantitative difference is that the damping timescale is slightly longer in radiative disks, because of the higher sound speed in an adiabatic gas. This is expected, since the damping is provided by backreaction of waves generated in the disk by an eccentric and/or inclined planet.

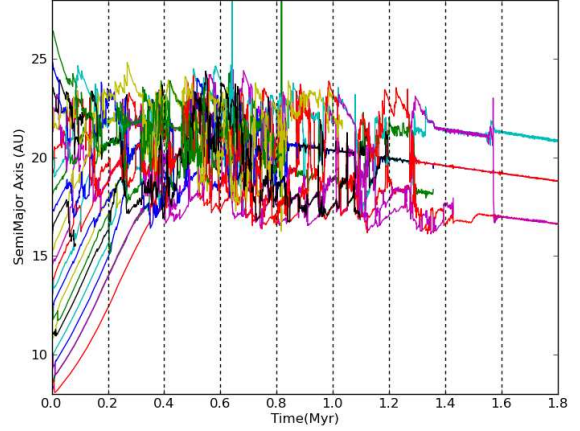


FIG. 2.— The history of our fiducial model (H1), initially consisting of 23 planetary embryos of $0.75M_{\oplus}$ each. The planets migrate towards the convergence zone. Chaotic N -body interactions then start, and continue until a massive core is formed. The planetary core eventually reaches a mass of $13M_{\oplus}$ and continues to occupy the zero-torque region, with smaller bodies interior and exterior to it being forced into mean-motion resonances.

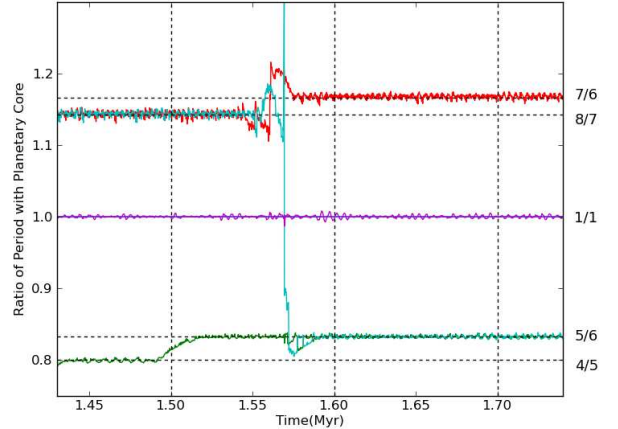


FIG. 3.— The fiducial model, (H1), creates a large core that eventually reaches a mass of $13M_{\oplus}$. The remaining bodies are trapped in resonances with the planetary core. Following the transition at 1.57 Myr, the resonances remain stable throughout the rest of the simulation, with two $3M_{\oplus}$ bodies trapped in the 5:6 resonance, a $6M_{\oplus}$ body in a 7:6 resonance, and a $3M_{\oplus}$ embryo trapped as a Trojan of the planetary core. Similar results are seen in other runs.

of the N -body integration, and the force from the damping effect on a planet moving with velocity v is calculated as

$$\mathbf{F}_{\text{damp},r} = -2 \frac{(\mathbf{v} \cdot \mathbf{r}) \mathbf{r}}{r^2 t_e} m_p \hat{\mathbf{r}} \quad (22)$$

$$\mathbf{F}_{\text{damp},z} = -\frac{v_z}{t_i} m_p \hat{\mathbf{z}}, \quad (23)$$

where $\hat{\mathbf{r}}$ and $\hat{\mathbf{z}}$ are the unit vectors in the r and z directions, respectively.

2.4. Turbulence

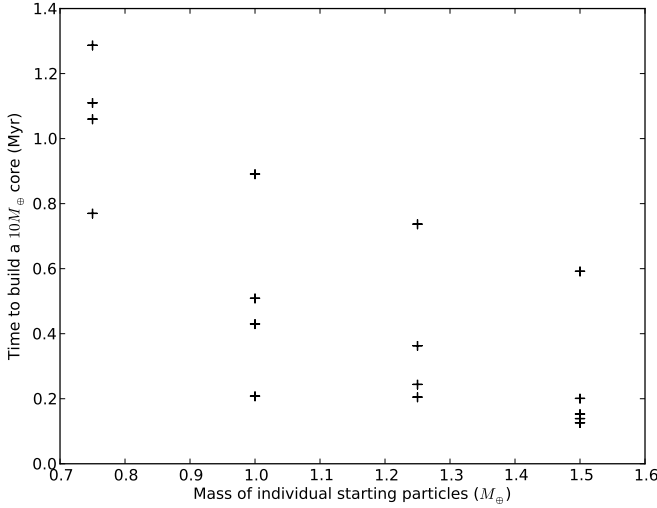


FIG. 4.— The time required to form a core of at least $10 M_{\oplus}$ is shown to be a function of the initial masses of the planetary embryos. These runs use a uniform mass for all bodies, whose value sets the x coordinate. All initial conditions except those for the $1.5 M_{\oplus}$ embryos have one simulation of the 5 runs fail to form a $10 M_{\oplus}$ core. These models are not included in the figure.

Small enough planets embedded in a turbulent disk have been shown to undergo random walks, rather than migrate inward in classical Type I migration (Nelson & Papaloizou 2004; Nelson 2005). The random walks can be modeled as a first order Markov process (Rein & Papaloizou 2009) where the root mean squared torque and the autocorrelation time can be calculated up to a constant by dimensional analysis. However, the correlation function of such a first order Markov process over the plane of the disk will be zero for all non-zero distances—so two planets in close proximity may feel completely different forces from this prescription for turbulence.

We use a model developed by Laughlin et al. (1994) and further modified by Ogiwara et al. (2007) that treats the turbulent force as the gradient of a potential multiplied by a scaling factor. In this model, the turbulent force is continuous over the disk and correlated torques act on planets near to each other. Due to the chaotic nature of N -body problems, turbulence can lead to collisions that would not have occurred otherwise, but during the close encounter of two bodies, the difference between the turbulent forces acting on each body goes to zero, and the relative velocity at collision is close to the velocity for two bodies on the same orbit in the absence of turbulence. Additionally, our results show that neighboring orbits near the convergence zone can be stable when separated by as little as 0.4 AU at a distance of 11 AU from the central star, so the same turbulent perturbations could affect both orbits.

The turbulent potential, Φ , is described as the sum of a large number of independent, scaled oscillation modes

$$\Phi_{c,m} = \psi r^2 \Omega^2 \Lambda_{c,m} \quad (24)$$

where $\Lambda_{c,m}$ is one oscillation mode, defined as

$$\Lambda_{c,m} = \zeta e^{-(r-r_c)^2/\sigma^2} \cos(m\theta - \phi_c - \Omega_c \tilde{t}) \sin\left(\pi \frac{\tilde{t}}{\Delta t}\right) \quad (25)$$

Each mode is defined by the azimuthal wavenumber

m , as well as r_c and ϕ_c , which specify the initial center of the mode. The magnitude of the perturbation is set by ζ , whose value is set by a normal distribution with standard deviation of 1 and a mean value of 0. The planet's location is given by the radial coordinates r and θ , and the displacement above the disk, z , is assumed to be small enough to have a negligible effect. The mode comes into existence at time t_0 and evolves as a function of $\tilde{t} \equiv t_0 + t$. The lifetime of the perturbation is $\Delta t = 2\pi r_c / (m c_s)$, which is the sound-crossing time for a mode, where c_s is the speed of sound. In Eq. (25), Ω_c is the Keplerian angular velocity at r_c .

The value for m is chosen from a log-random distribution ranging from 1 to 64. The value of r_c is selected from a uniform random distribution ranging from r_{int} to r_{ext} , and ϕ_c is selected from a uniform distribution from 0 to 2π . The radial profile of the perturbation is a Gaussian whose size is set by $\sigma = \pi r_c / (4m)$. At the beginning of a simulation, n independent modes are generated, and as one mode expires another is generated so that at any time there are n perturbations. This parameter n is set to 50 in Laughlin et al. (1994) as well as in Ogiwara et al. (2007), but since we are investigating a disk that is an order of magnitude larger than that in Laughlin et al. (1994), we have included 100 modes.

In Eq. (24), the magnitude of the potential used to model turbulence is determined by the dimensionless parameter ψ . This sets the scale for the magnitude of the turbulent force in comparison to the laminar forces due to Lindblad resonances and horseshoe torques. Ogiwara et al. (2007) suggest that ψ can be anywhere from 10^{-3} to 10^{-1} , depending on the strength of the instability driving the turbulence. The relation between ψ and the Shakura & Sunyaev (1973) α parameter was explored in Baruteau & Lin (2010). Baruteau & Lin (2010) found that

$$\psi \approx 8.5 \times 10^{-2} h \sqrt{\alpha} \quad (26)$$

where the h term enters due to the mode lifetime being set by the speed of sound. Our model does not have a constant value for h , but we set this to 0.05 in this relation. We use two disks in our simulations, with α values of 10^{-2} and 10^{-3} , so following Baruteau & Lin (2010), we take $\psi 4.25 \times 10^{-4}$ and 1.34×10^{-4} , respectively.

The sum of the n independent oscillations, $\Phi_{c,m}$, specifies the shape of the potential, $\Phi = \sum \Phi_{c,m}$, that, in Laughlin et al. (1994), acted on the gas to generate density perturbations, which in turn applied a force to the planet. We do not apply the potential to our gas disk, which is only evolved in one dimension. Instead, the potential is used to calculate the force acting on the planet directly. Ogiwara et al. (2007) state that the force from such a turbulent disk can be expressed as

$$\mathbf{F}_{\text{turb}} = -C \nabla \Phi \quad (27)$$

where C relates the size of the force acting from the potential onto the gas to the size of the force acting from the gas onto the planet

$$C = \frac{64 \Sigma r^2}{\pi^2 M_*} \quad (28)$$

The strength of the force scales with the surface density of the gas at the planet's location, $\Sigma(r)$. Eq. (27) can

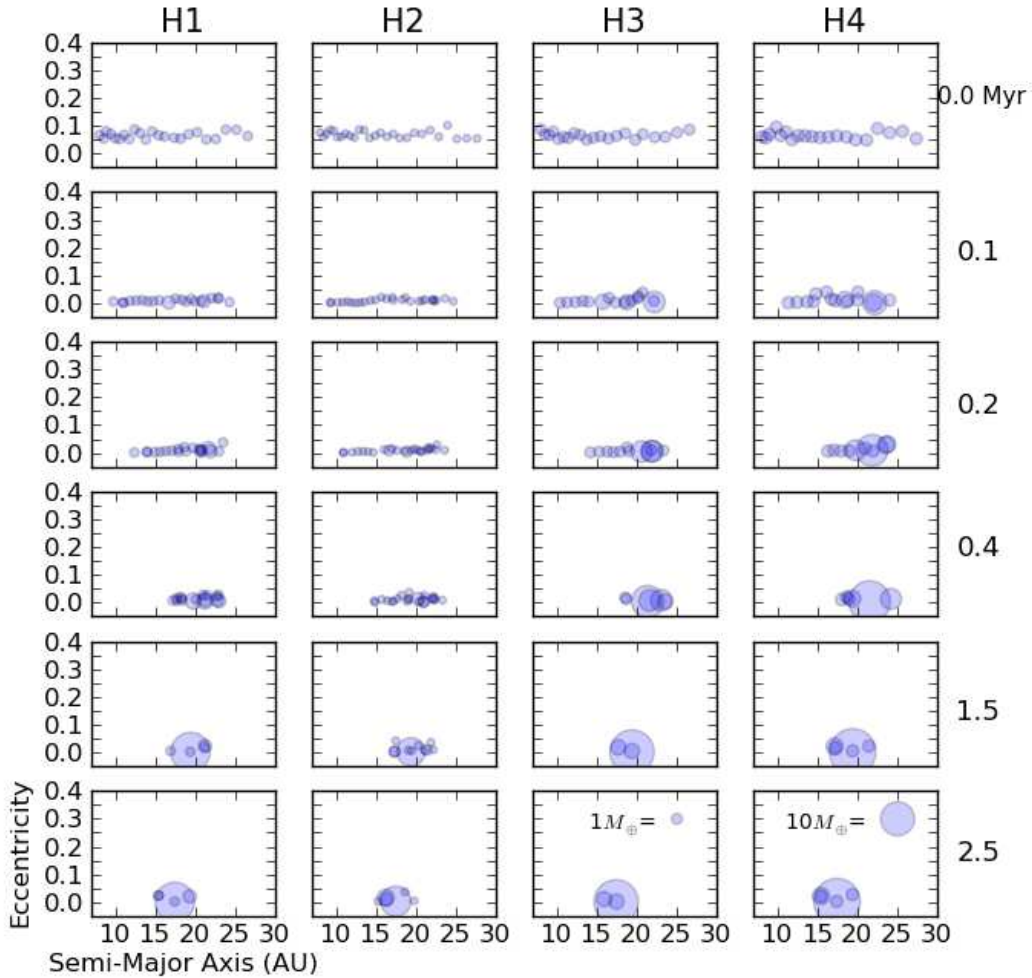


FIG. 5.— Time histories of models H, which initially consist of planetary embryos with 0.75 , 0.5 , 1.0 and $1.25 M_{\oplus}$, respectively. Each row depicts all four runs at a given time in its history—the top row represents the initial conditions, followed by 0.1 , 0.2 , 0.4 , 1.5 , and 2.5 Myr. Each panel depicts the semi-major axis and eccentricity of the bodies, with the area of a body scaling linearly with mass. Circles corresponding to masses of $1M_{\oplus}$ and $10M_{\oplus}$ are shown for comparison in the bottom row. All but the $0.5 M_{\oplus}$ run H2 form a core of at least $10 M_{\oplus}$ by 1.5 Myr

be used to calculate the force due to turbulent perturbations on a planet at position (r, θ) at time t . Ogiwara et al. (2007) showed that all modes with wavenumbers higher than 6 can be left out of the summation to determine the potential Φ , and so we follow this simplification, including only perturbations where $1 \leq m \leq 6$ in our calculation of Φ .

2.5. *N*-Body Code

We simulate the behavior of multiple planetary embryos approaching a convergence zone, using the Bulirsch-Stoer *N*-body code described by Sándor et al. (2011), modified to include the additional forces from the gas disk on each body. The temperature and surface density profiles from the one-dimensional hydro simulations conducted previously are read into the *N*-body simulation at each timestep and used in the prescriptions described in Sections 2.2, 2.3, and 2.4 to determine the additional forces.

The total force resulting from Type I migration, damping, and turbulence are computed for each body at the beginning of a Bulirsch-Stoer timestep, but are held constant in each refinement of the modified midpoint algorithm during a given Bulirsch-Stoer timestep. The Bulirsch-Stoer timesteps are a small fraction of the dynamical time of the bodies, and are reduced during close encounters, so the simplification of holding these forces constant during a timestep does not change the overall behavior of the bodies. The net force acting on a body is given by

$$\mathbf{F}_{\text{total}} = \mathbf{F}_{\text{nbody}} + \mathbf{F}_{\text{typeI}} + \mathbf{F}_{\text{damp}} + \mathbf{F}_{\text{turb}} \quad (29)$$

where $\mathbf{F}_{\text{nbody}}$ represents the gravitational forces from the other bodies and the central star. The net force from the migration torques is

$$\mathbf{F}_{\text{typeI}} = \frac{\Gamma_{\text{typeI}}}{r} \hat{\boldsymbol{\theta}}, \quad (30)$$

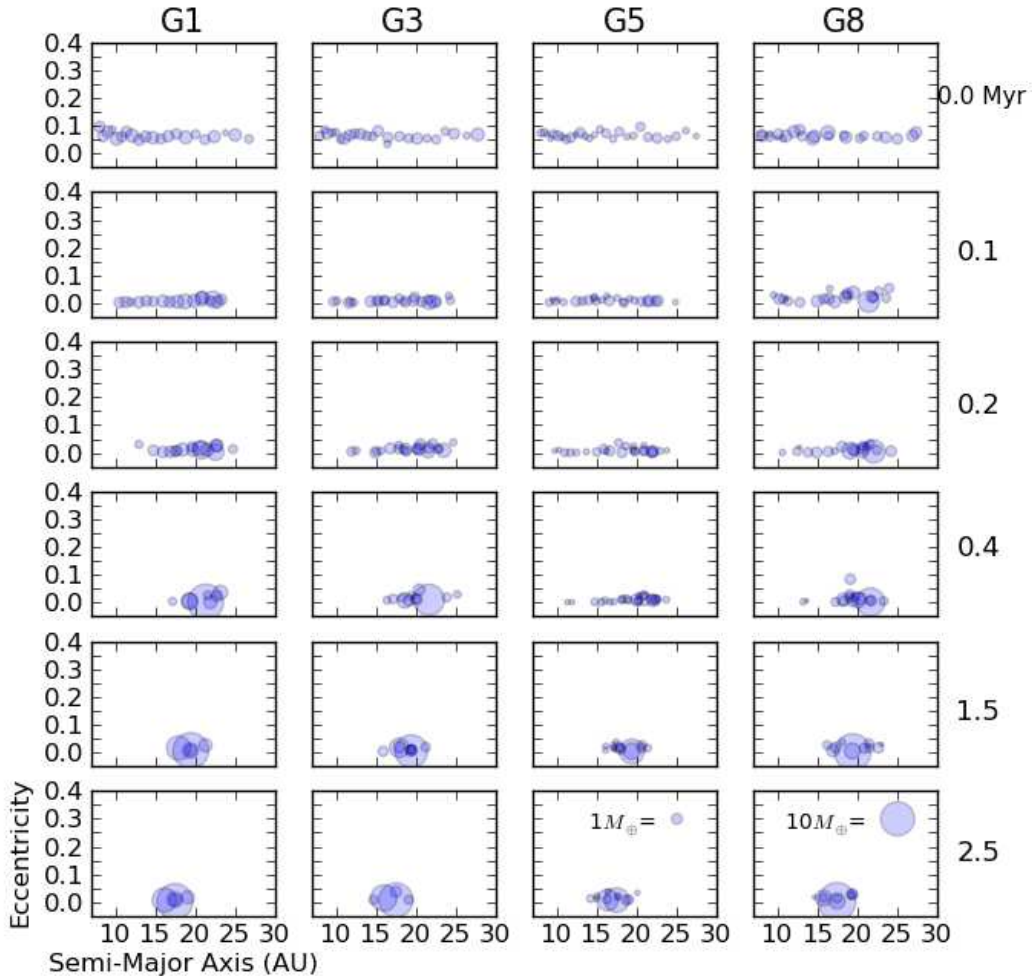


FIG. 6.— Time histories of runs with a Gaussian mass distribution centered at $1.0M_{\oplus}$ (model G1), $0.75M_{\oplus}$ (G3), and $0.5M_{\oplus}$ (G5) are presented, along with a superimposed distribution of the low density populations G2 & G4 (G8). The top row shows the initial conditions, followed by the system after 0.1, 0.2, 0.4, 1.5 and 2.5 Myrs. The results of core formation, and the time required to build a core, are comparable for the Gaussian and uniform mass distributions.

while the components of F_{damp} are given by Eqs. (22) and (23), and F_{turb} is derived in Eq. (27).

A collision occurs if two bodies pass within a distance equal to the sum of the radii of the two bodies, where the radii are derived by assuming that all bodies have a bulk density of 2 g cm^{-3} . Collisions result in the formation of one body with a mass and momentum equal to the sum of the two colliding bodies. This approximation is appropriate for bodies with the masses of planetary embryos that have escape velocities substantially exceeding typical collision velocities.

3. INITIAL CONDITIONS

3.1. Gas Disk Parameters

The evolution of the gas disk was described in Sect. 2.1. The parameters that set the initial profile of disk density and temperature are α , which sets the viscosity, the background temperature, T_b , and the mass

accretion rate, \dot{M} . MHD simulations consistently suggest that α has a value of 10^{-2} (e.g. Davis, Stone & Pessah 2010), though if the migration is taking place in a dead zone, the viscosity should be smaller, though non-zero (Fleming & Stone 2003; Oishi and Mac Low 2009). Our simulations use a disk with $\alpha = 10^{-2}$, an accretion rate $\dot{M} = 10^{-7} M_{\odot} \text{ yr}^{-1}$, an external radius $r_{\text{ext}} = 30 \text{ AU}$, and $T_b = 10 \text{ K}$. The parameters for the gas disks used in our simulation are set so that the convergence zone lies within the simulation at all times.

The photoionized wind has an escape radius $r_g = 5 \text{ AU}$ for a $1 M_{\odot}$ star, and a photoevaporation rate set by a mass loss rate from the disk of $\dot{M}_w = 3 \times 10^{-8} M_{\odot} \text{ yr}^{-1}$. The accretion rate \dot{M} , along with the photoevaporation rate \dot{M}_w and radius r_g , determines the lifetime of the disk. Using the given values for our parameters yields a $0.08 M_{\odot}$ disk with an 8 Myr lifetime.

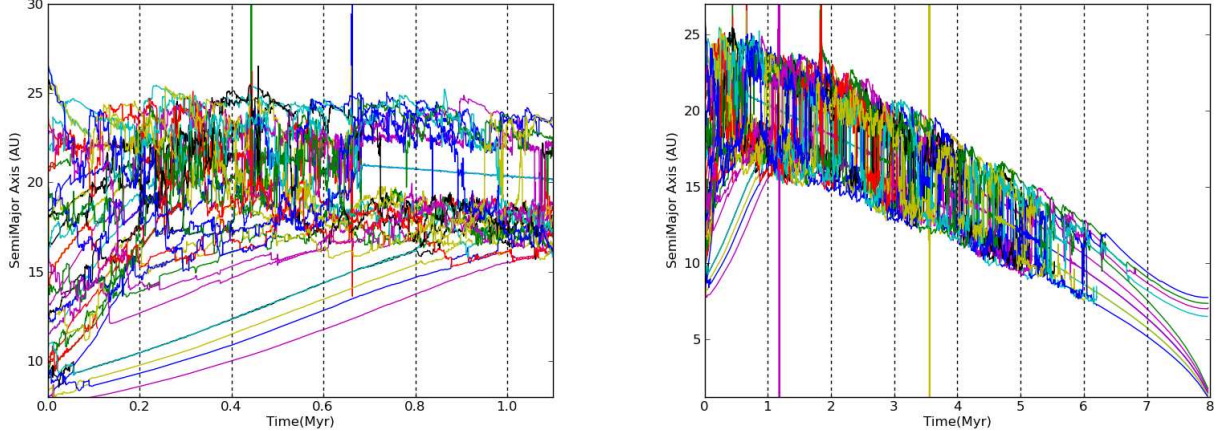


FIG. 7.— *Left panel.* The formation history of model Sw3, which has 11 $1M_{\oplus}$ bodies, migrating through a population of 25 $0.25M_{\oplus}$ bodies. The massive bodies do not merge with the lower-mass ones as the massive bodies rapidly migrate towards the convergence zone. Low mass bodies are briefly scattered, but then resume their slower migration rate. The massive bodies finish migrating to the convergence zone by 0.3 Myr, while the low-mass bodies continue to migrate until 1.0 Myr. An $8.5 M_{\oplus}$ core is formed, though only two of the 25 $0.25M_{\oplus}$ bodies are consumed in forming it. *Right panel.* Extended history of the model. The swarm of smaller particles is seen to be long lived compared to the time required to form a planetary core. The swarm of low mass embryos does eventually merge with other bodies as they migrate inwards.

3.2. Planet Embryos

The location of the convergence zone, where $F_{\text{typeI}} \rightarrow 0$, is determined by an opacity transition that in turn is set by the background temperature and the viscosity of the disk. In a disk with $T_b = 10\text{K}$ and $\alpha = 10^{-2}$, the convergence zone begins near 22 AU and moves inwards towards the star on the viscous evolution timescale. Since this is the region of interest, and the computation time using the Bulirsch-Stoer method scales as the number of bodies squared, we distribute the initial semi-major orbital radii of planet embryos uniformly around the radius of the convergence zone. Most runs begin with planetary embryos in the region between 8 and 28 AU.

A consensus has not been reached on the initial mass function of planetary embryos. Starting with an initial population of 3000 equal mass (10^{23}g) seed planetesimals, and assuming a growth process dominated by binary collisions in the absence of gas drag and fragmentation, Kokubo & Ida (1996) find a resulting mass distribution of power-law index 2.5 ± 0.4 . The result of the opposite process, a collisional cascade from fragmentation of a parent body or collection of parent bodies with subsequent self-similar grinding of the fragments, yields a quasi-steady mass distribution of power law $11/6$ (Dohnanyi 1969; Tanaka et al. 1996). Lyra et al. (2008) found from hydrodynamical models of protoplanetary disks including interacting decimeter-sized particles and gas tides, that the resulting mass distribution of lunar and Mars-sized embryos obeyed a power-law index of 2.3 ± 0.2 , consistent with coagulation (Kokubo & Ida 1996) and, at 3σ , with fragmentation (Dohnanyi 1969), suggesting a combination of both processes. However, none of these power laws match the observed mass distribution of the Asteroid and Kuiper belts (e.g., Cuzzi et al. 2010; Morbidelli et al. 2009), which are characterized by multiple power-laws (see fig 1 of Morbidelli et al. 2009). Instead of adopting these

power-laws, we use simple mass distributions, detailed below. We justify this by noting that the relaxed mass distribution is nearly independent of the initial mass distribution (Kokubo & Ida 1996). The parameters of the various models we ran are shown in Table 1. We detail them in this and in the next section.

First, in our fiducial model (model H1 in Table 1), the initial masses of the planetary embryos are all set to $0.75 M_{\oplus}$. The innermost embryo is placed in a circular orbit with radius $a_1 = 8\text{AU}$, and each successive embryo is placed so that neighbors i and j are initially separated by $N \times R_{mH}$, where the mutual Hill radius

$$R_{mH} = \left(\frac{m_i + m_j}{3M_{\star}} \right)^{1/3} \left(\frac{a_i + a_j}{2} \right), \quad (31)$$

and $a_j = a_i + N R_{mH}$. In the fiducial model H1, we use $N = 3$. Several other runs were performed with varying masses of initial bodies, but maintaining the constraint of spacing consecutive bodies by three mutual Hill radii. These runs are all labeled *H*, for “Hill spacing”, in Table 1.

Second, we used a Gaussian distribution of the initial masses of planet embryos. This is done by setting the mean mass and standard deviation for the distribution, with a floor of $0.1 M_{\oplus}$ and a ceiling of $2M_{\oplus}$. These models are labeled *G*, for “Gaussian”, in Table 1. In these runs, the mutual Hill radii constraint is still used to determine initial locations, but the number of Hill radii between neighboring bodies is varied between runs to model low density and high density populations. Three further simulations are performed with an initial population of bodies resulting from superimposing two low density populations (models G7–G9).

Third, we ran initial conditions consisting of two populations of planetary embryos with different masses, to investigate how massive, quickly migrating bodies interact with lower-mass bodies that migrate on much longer timescales. The low-mass population in this

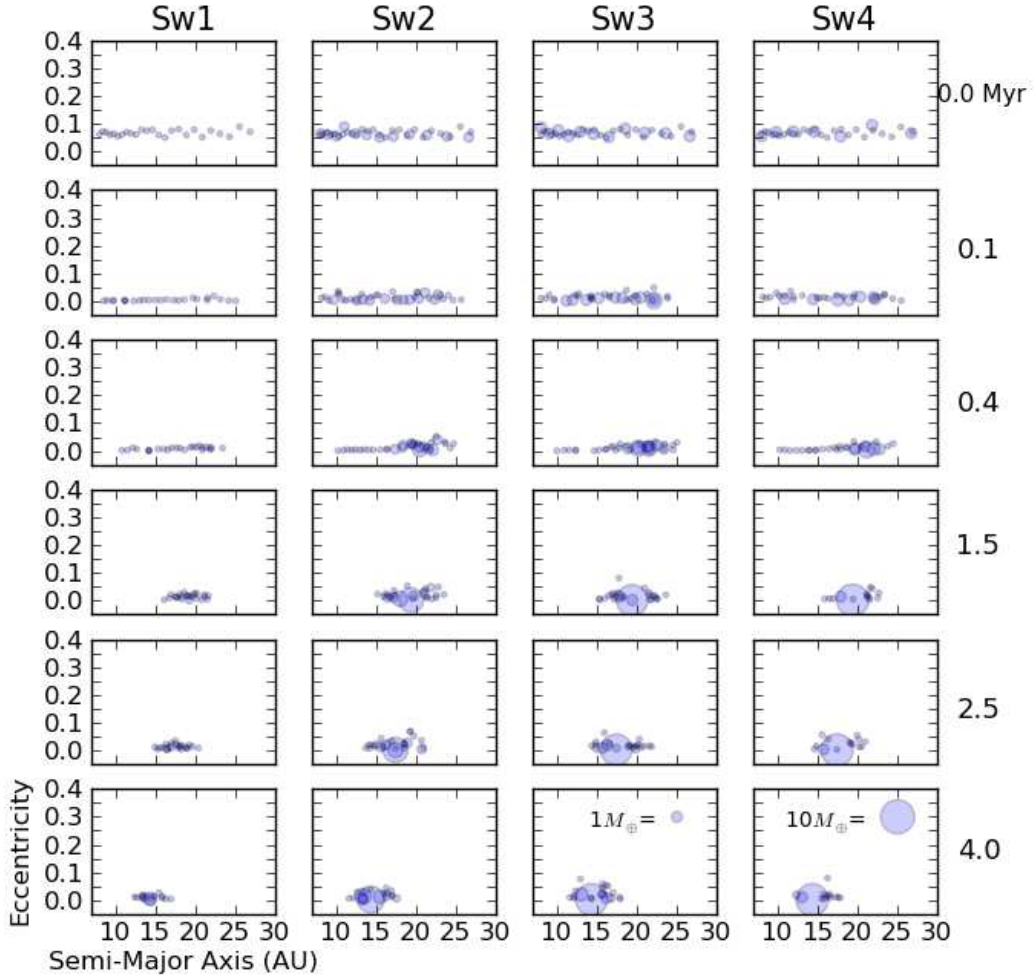


FIG. 8.— Simulation histories of models *Sw*, where a population of planets evolves while interacting with a swarm of 25 low-mass ($0.25 M_{\oplus}$) embryos. Column 1 shows the evolution of the swarm alone (model *Sw1*). The more massive bodies quickly migrate to the convergence zone where they begin to form a planetary core. Only a small number of the $0.25 M_{\oplus}$ bodies collide with anything, while most follow chaotic orbits in two distinct clusters, one interior and one exterior to the planetary core. These swarms eventually merge at later times, as seen in Fig. 7.

model consists of 25 embryos with a mass of $0.25 M_{\oplus}$ separated by 4 mutual Hill radii, while the massive population consists of planets with masses of 0.75 or $1.0 M_{\oplus}$ separated by either 6 or 10 mutual Hill radii. The two populations are generated independently of one another, so a large and small body may initially be in close proximity to one another. These models are labeled *Sw*, for “swarm”, in Table 1.

Fourth, we use an initial configuration that scales with the amount of disk mass within the orbital radius of a planetary embryo. The mass of the planetary embryos is held constant, so the initial spacing between the semi-major axes of neighboring embryos is varied so that the mass of the gas in the annulus separating the two bodies is constant. Assuming that the dust-to-gas ratio in the disk is 0.01, and planetesimal formation turns 15% of the dust into planetary embryos, then the initial spac-

ing between two neighboring bodies

$$\Delta r = (6.67 \times 10^2) \frac{M_p}{2\pi r \Sigma}. \quad (32)$$

where the numerical factor is the inverse of the product of the dust-to-gas ratio 0.01 and the planet formation efficiency 0.15. These models are labeled *SD*, for “surface density”, in Table 1. One simulation is performed using a Gaussian mass distribution, spaced using the *SD* criteria. This simulation is included in the *SD* suite of simulations.

The initial eccentricities and inclinations of planets are also selected randomly from Gaussian distributions. The inclination is the absolute value of a Gaussian distribution with 0 mean and 0.05° as the standard deviation. The mean value for the initial eccentricity is 0.05, with a standard deviation of 0.02. If the eccentricity is negative, a new value is generated until the value is non-negative. Due to the magnitude of the damping

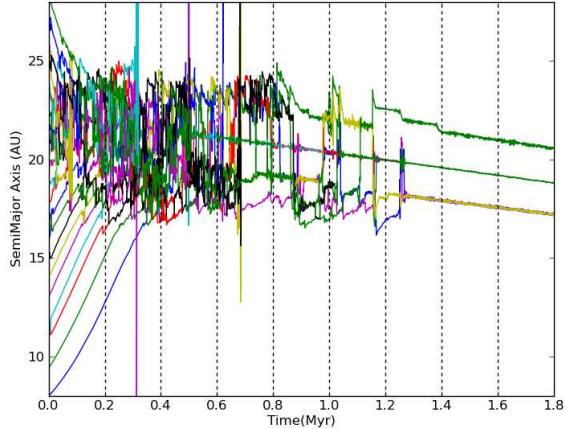


FIG. 9.— The history of model SD1, a run with $0.75M_{\oplus}$ planets initially distributed such that the surface density of planets is 0.15% of the gas surface density. The results are comparable to the fiducial model, suggesting that mass distribution does not alter the qualitative description we have given of the formation of planetary cores.

force, initial eccentricities and inclinations are found to be transient and do not play a significant role in the simulations.

4. RESULTS

4.1. The Fiducial Model

The history of the fiducial model (H1), with 23 bodies each having a mass of $0.75M_{\oplus}$ and separated by $3R_{mH}$, is shown in Fig. 2. Initially, the motions of the embryos are dominated by the Type I torque, leading to rapid convergence. The convergence leads to close encounters between neighboring bodies, resulting in collisions and orbit swapping. The close encounters and chaotic scattering and collisions persist until the number of remaining planets is small enough to quiescently migrate inwards.

The sharp peaks near 600,000 and 800,000 years are not planets being scattered out to large radii, but rather the result of solving for the orbital elements, assuming the planet is orbiting the central body, when in reality the bodies have formed a transient binary system. Such binary systems and satellite capture have been observed in other N -body simulations that include the effects of a gas disk, such as Cresswell & Nelson (2008).

The fiducial model has a total initial mass of $17.25M_{\oplus}$ in planet embryos. In it, a $10.5M_{\oplus}$ core forms at the zero-torque orbit in 1.29 Myr. No further collisions happen after this, as the remaining bodies are trapped in mean-motion resonances with the massive planetary core (Fig. 3). Two $3M_{\oplus}$ bodies are trapped in the 5:6 resonance with the planetary core, and a $6M_{\oplus}$ body is trapped outside the orbit of the planetary core, in a 7:6 resonance with it. An additional $3M_{\oplus}$ embryo orbits within the co-orbital region of the planetary core as a Trojan. Other simulations show similar behavior, with accretion eventually being halted by resonance trapping once the planetary core is massive enough.

4.2. Variations of Planetary Embryo Mass

The fiducial model begins with planetary embryos of $0.75M_{\oplus}$. We also simulate disks populated with embryos of 0.5 , 1.0 , 1.25 , and $1.5M_{\oplus}$ separated, as in the fiducial case, by $3R_{mH}$. These correspond to models H2-H5 in Table 1. Given the dependence of the Hill radius on the mass of the planet, systems consisting of more massive embryos contain a greater total mass.

Since the magnitude of the migration torque, Eq. (12), varies as the square of the mass of the planet, and thus the acceleration varies linearly with mass, lighter embryos take longer to migrate to the convergence zone. This, combined with gravitational focusing, explains why the time required to build a core is a strong function of the initial mass of the embryos (Fig. 4). The fiducial model built a $10M_{\oplus}$ core in 1.28 Myr, while the run using $1.0M_{\oplus}$ embryos reached a $10M_{\oplus}$ core in 0.43 Myr. The runs with 1.25 and $1.5M_{\oplus}$ embryos formed cores in 0.21 and 0.15 Myr, respectively. The $0.5M_{\oplus}$ embryos failed to produce a $10M_{\oplus}$ body, but did form an $8M_{\oplus}$ core after 2.22 Myr.

To see if these results are characteristic of such a mass distribution, identical simulations to the ones above with initial planet masses of 0.75 , 1.0 , 1.25 , and $1.5M_{\oplus}$ are run, though the azimuthal distribution of the planets is varied, and so the chaotic interactions lead to different results. The dependence of the time required to assemble a massive core does hold for the five runs of each initial mass. There is, however, a wide upper bound for the time to form a core, so much so that each distribution other than the $1.5M_{\oplus}$ runs (model H5) had one run of the 5 fail to form a $10M_{\oplus}$ core. These are not plotted in Fig. 4, but the resulting systems were interesting, often consisting of two or more massive bodies coorbiting with one another stably for the rest of the 8 Myr simulation.

The formation history of runs H1-4 are shown in Fig. 5. The simulations with more massive embryos are seen to rapidly develop large planets, while the simulations consisting of embryos with initial masses less than $1M_{\oplus}$ remain dispersed after 4×10^5 yr. The simulations demonstrate that, while the time required to form a core can vary by over an order of magnitude for embryos whose initial mass differs by a factor of two, the resulting core and the arrangement of the remaining bodies is similar for all the simulations. The results presented in Fig. 5 are representative of the collection of simulations run with these initial conditions.

Runs G1-9 also suggest that the rate of core formation is highly dependent on the mass of the embryos. Two runs with a mean mass of $1.0M_{\oplus}$ and a standard deviation of $0.3M_{\oplus}$ (G1 and G2) built large cores within 0.3 Myr. The initial masses for the two distributions are generated independently, which also varies the radial distribution, since planets are initially separated by $3R_{mH}$. The core formation history of one of these runs is shown in Fig. 6, along with the formation histories of G3, G5, and G8. The results of these runs suggest that the trend seen in Fig. 4 can be used to estimate the time required to assemble a core from a Gaussian mass distribution with a given mean mass.

If the mean of the initial mass distribution is lowered to $0.5M_{\oplus}$ (models G5 and G6) the time required to migrate bodies to the convergence zone increases signifi-

cantly, and when cores are built, they are smaller and take longer to form. The mass distribution is again Gaussian with a standard deviation of $0.2M_{\oplus}$, though there are lower and upper mass limits of $0.1M_{\oplus}$ and $2.0M_{\oplus}$, respectively. Two runs were performed, with an independent mass distribution generated for each. The first run took 2.5 Myr to build a $6.9M_{\oplus}$ core, and is depicted in Fig. 6 beside the history of a run composed of only $0.5M_{\oplus}$ planetary embryos. The second run took 3.2 Myr to form a $9.3M_{\oplus}$ core.

The runs with a population of $0.25M_{\oplus}$ bodies interspersed with more massive embryos did not result in the smaller bodies being swept up in collisions with the rapidly migrating large embryos. Instead, the larger embryos scatter the $0.25M_{\oplus}$ objects into high eccentricity orbits and continue to migrate towards the convergence zone where mergers between large bodies go on to create cores. This can be seen in Fig. 7 (left panel) by the two characteristic timescales for migration, which, aside from a few brief scattering events, occur more or less independently of one another. Following the formation of a core with mass $\sim 5M_{\oplus}$, smaller bodies are seen to collide with the core or become trapped as Trojans. Many, though, avoid close encounters with the planetary core and continue to interact chaotically with the other remaining small planetary embryos in two swarms, one interior and one exterior to the planetary core. Neglecting the (substantial) effect of gas accretion onto the planetary core, the model shows that these swarms eventually merge at later times, as seen in the right panel of Fig. 7, which depicts the whole 8 Myr of the simulation. Figure 8 depicts the evolution of the background swarm of $0.25M_{\oplus}$ by themselves (model Sw1) as well as three cases where more massive bodies are interspersed into the low mass swarm (models Sw2-Sw4). The mass of the larger bodies, as well as the number of larger bodies, is not seen to have a noticeable effect on the migration and merging of the smaller bodies.

4.3. Mass Distribution

An alternative to determining the initial positions of planetary embryos by requiring them to be a set number of mutual Hill radii from their neighbor is to require that the distribution of mass in the form of planets mirror the mass distribution of the gas disk. This leads to a larger number of planets starting at radii exterior to the zero-torque orbit. In Fig. 9, we compare the history of fiducial run H1 with run SD1, which differs from the fiducial run only in that the planetary mass is linearly proportional to the mass of gas within an annulus, following Eq. (32).

The early period of convergence is skewed to larger radii in the latter, but as can be seen in Fig. 1, the torque exterior to the convergence zone is of the same magnitude as the torque interior to the convergence zone. The time to migrate from initial locations to close enough to the convergence zone that N -body effects take over is not significantly affected by altering the initial radial distribution of planets.

5. CAVEATS

The prescription for Type I migration used in this paper was derived by Paardekooper et al. (2010) using 2D

simulations. Those authors noted that the gas dynamics may act differently in 3D.

Our simulations assume that the Type I migration torque derived for an isolated body in a non-isothermal disk also applies to many bodies that pass arbitrarily close to one another. This close proximity may significantly alter the migration torque or lead to a more rapid saturation of the torque. Such proximity is often short-lived, but in the case of a satellite being captured could lead to a change in the torque acting on the pair lasting thousands of years. A preliminary two-dimensional hydrodynamical simulation of two bodies migrating in close proximity suggests that the wakes of the planets drive brief periods of large variations in the torque. This will be explored in future work.

The initial convergence takes place while planets are separated from one another, so using the prescription for the torque on an isolated body is reasonable. Following convergence, close gravitational encounters dominate until a planetary core is formed. In several simulations, the resulting system had two large bodies that had a combined mass greater than $10M_{\oplus}$ but failed to produce a single massive core. Studying such a system in a simulation that accounts for gap opening by the planets in the gas disk could shed light on how such an arrangement will evolve.

Bitsch & Kley (2010) showed that the horseshoe torque is reduced as eccentricity is increased, and shuts down as the radial excursions associated with eccentricity exceed the width of the co-rotation region. Bitsch & Kley (2011) further showed that outward migration can be sustained for inclinations up to about 4.5° , after which migration stalls in general, owing to the lower densities away from the disk midplane. We assess the effect of eccentricity and inclination in the next section.

In addition, the prescription for the co-rotational torque that we use considers only the unsaturated regime. We calculate for the parameters used in the present work that the effects of diffusion, explored in Paardekooper et al. (2011) for alpha disks, imply that only larger planets, with masses exceeding $\approx 4M_{\oplus}$, will experience sustained outward migration. Our choice of working with the unsaturated torque stems from the results of Baruteau & Lin (2010), Uribe et al. (2011), and Baruteau et al. (2011). These works measured the co-rotational torques in turbulent disks, finding that the stochastic turbulent fluctuations work toward keeping the co-rotational torque unsaturated even in locally isothermal simulations. Baruteau et al. (2011) have conclusively shown that horseshoe dynamics exists in turbulent disks, and argue that it occurs when the amplitude of the U-turn drift rate exceeds that of the turbulent velocity fluctuations. This condition may or may not occur for smaller planets, for which the U-turn drift rate is reduced. Unfortunately, neither Baruteau et al. (2011) nor Uribe et al. (2011) could numerically resolve the expected horseshoe region width in this mass range. We thus recognize saturation for smaller planets as a possibility, but regard the question as unsettled.

Our conclusions about resonance trapping neglect the effect of interactions with the wakes of the growing planetary core. These may be sufficiently strong to knock lower-mass bodies out of the resonances that we find. Even if the resonances do remain, our assumption

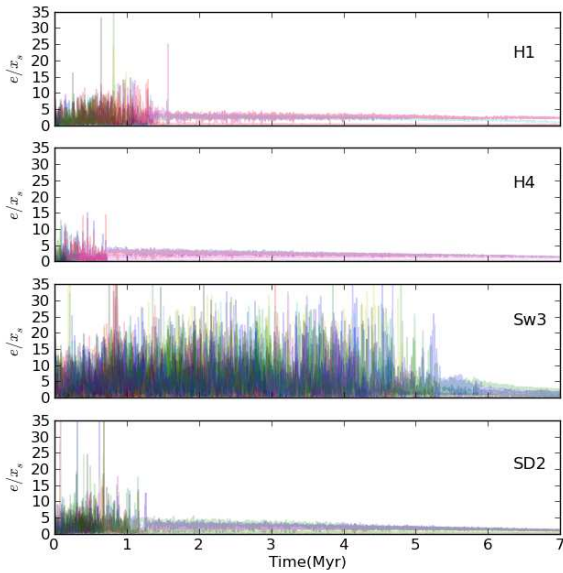


FIG. 10.— The eccentricity e normalized by the dimensionless half-width of the co-rotational region x_s , for the protoplanets in four of our models. The eccentricity is pumped well above the critical value of $e/x_s = 1$ associated with shutdown of the horseshoe drag (see text).

about evolving the gas disk independently of the planets breaks down once the planetary core has reached a mass near $10 M_{\oplus}$. At that point it begins first to accrete gas, and then, when its Hill radius exceeds a disk scale height, to open a gap in the disk. Our models account for neither development, and so should be taken as only qualitatively indicative (e.g. the right panel in Figure 7) after any object reaches this mass.

We note that the actual critical mass necessary for runaway gas accretion is a sensitive function of the luminosity of the forming planet, which is determined by the release of gravitational binding energy of the accreted material—usually assumed to be provided steadily by planetesimals. In our model, this continuous luminosity is essentially zero, which would lead to a very small critical core mass (Papaloizou & Terquem 1999). The energy is instead provided in discrete violent collisions. A model that incorporates a self-consistent treatment of gas accretion and gap formation by a growing planet with envelope luminosity provided by both planetesimal accretion and binary collisions would be required to fully assess the initial stages of giant planet formation.

5.1. Comparison to Recent Work

The work presented in this paper examines the same regime as that studied by HN12, which was made public after the initial submission of our work. Although both works deal with the impact of co-rotation torques and convergent migration on the growth of protoplanets, there are differences in the models that are worth highlighting, in order to understand the different results obtained.

First, we discuss the gas evolution model. In the present work we model the gas density by equating the

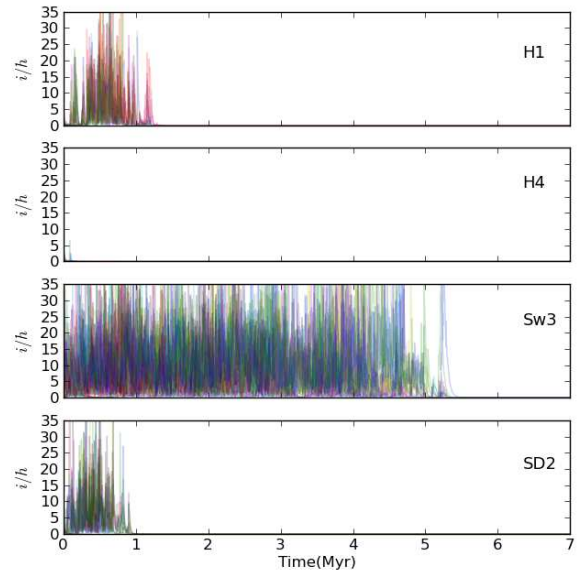


FIG. 11.— The inclinations i normalized by the aspect ratio h of the disk, for the same models as in Fig. 10. The inclinations are pumped well above the critical value of $i_{\text{crit}} = 0.08$ (i.e., $i_{\text{crit}}/h = 1.6$) beyond which migration stalls (see text). This is a potentially important phenomenon, perhaps countering the shutdown of co-rotational torques due to finite eccentricity shown in Fig. 10.

radial velocity with the viscous inflow, the azimuthal velocity with the Keplerian value, and solving the resulting diffusion equation in the presence of photoevaporation. The initial condition for density is set by defining a global value for mass accretion rate and viscosity (α) value, which in turn define the surface density (Papaloizou & Terquem 1999). Having defined the density, the disk is assumed to maintain thermal equilibrium between heating by viscous dissipation and cooling via black body radiation in a background radiative field of temperature T_b , according to equation (5). In HN12, the density and temperatures are set as global power-laws (that may drop well below the physical value of $T_b \approx 10$ K set by the surrounding molecular cloud, and even below the temperature of the cosmic microwave background). The viscous-photoevaporative evolution of the density is mimicked by an exponential decay with a fixed e-folding time τ_{disk} ; the temperature is evolved dynamically assuming thermal diffusion in the radial direction.

Next we consider the growth of the protoplanets. While our work concerns the formation of a core of a giant planet in the vicinity of a convergent migration zone via binary collisions, HN12 attempt a more comprehensive approach. In addition to collisions with planets of terrestrial size, their protoplanets also accrete from a disk of 10 km planetesimals subject to Stokes drag. They also include an approximate scheme for gas accretion based on fits to the fast 1D giant planet formation model of Movshovitz et al. (2010). In their model, gas capture is a function only of core mass and time, starting at roughly $3 M_{\oplus}$, with runaway gas accretion setting in at $30 M_{\oplus}$. The gas accretion is artificially cut off at either

the Jovian mass or at the gas isolation mass, whichever is lower.

A minor difference between our work and HN12 lies in the inclination and eccentricity damping. Both works use prescriptions that are based on the analytical formulae derived by Tanaka et al. (2002) and Tanaka & Ward (2004). HN12 use the same inclination damping, but a smoother version for eccentricity damping. We use the model of Cresswell & Nelson (2008) that improves on Tanaka & Ward (2004) by including empirical fits to the transition from exponential to quadratic damping at higher eccentricities and inclinations.

Finally we consider the prescription for migration of the protoplanets. HN12 model saturation effects, while we chose to work with the fully unsaturated torque, as explained in the previous subsection. Another major difference is our inclusion of stochastic migration (Nelson & Papaloizou 2004; Nelson 2005) caused by the inclusion of turbulent jitter (Sect. 2.4).

As a result, HN12 find a bimodal formation process. Cores that grow too massive too fast migrate into the star, whereas cores of moderate mass slowly migrate outward to large distances, accreting gas and becoming giant planets at wide orbits, mostly beyond 10 AU. Super-Earths or Neptune-mass planets were not easily formed.

The difference in the results that we find are readily understood in terms of these differences in the modeling. First, without a background radiation field of temperature T_b below which the disk cannot cool, the model of HN12 lacks the transition to isothermality that gives rise to a limit of outward migration in our models, usually between 10–20 AU, depending on the initial parameters used. Second, their inclusion of saturation in HN12 introduces a mass-dependency to both the location and existence of convergence zones. Rapid inward migration occurs for planets outside of a narrow range in mass. Lastly, our inclusion of turbulent jitter dynamically excites the resonant convoy, leading to more gravitational interaction than seen in HN12, and faster core growth. These differences highlight the fact that planet migration and growth depend very sensitively on the disk model adopted.

In two out of their suite of forty simulations, HN12 apply a eccentricity cutoff to the co-rotational torque, taking in to account the findings of Bitsch & Kley (2010). They find that the eccentricity excursions of the protoplanets easily exceed the threshold of $e/x_s = 1$, where $x_s = 1.1/\gamma^{1/4}\sqrt{q/h}$ is the dimensionless half-width of the co-rotational zone, therefore quenching the co-rotational torques. We measure e/x_s in four of our models. The result is shown in Fig. 10. We see that the eccentricities excited by the N-body interactions and the turbulent jitter on the protoplanets far exceeds the stringent threshold of $e/x_s = 1$, confirming the result of HN12. However, the same processes that account for eccentricity pumping should also lead to inclination growth. As shown by Bitsch & Kley (2011), migration stalls in general when the inclination rises above a threshold $i_{\text{crit}} \approx 4.5^\circ \approx 0.08$. We plot in Fig. 11 i/h for the same models as in Fig. 10. A comparison of the two figures suggests that eccentricity and inclination are indeed correlated. The aspect ratio being $h = 0.05$, we have $i_{\text{crit}}/h = 1.6$. Figure 11 shows that the inclinations

grow well beyond this modest threshold. This indicates that although the high eccentricities would lead to a shutdown of the co-rotational torques and resuming of fast inward migration, the associated high inclinations would mitigate the effect by also shutting down the Lindblad torque and, consequently, migration in general.

6. CONCLUSIONS

We have studied the evolution of multiple planets migrating in a non-isothermal gas disk, assuming unsaturated migration torques (Paardekooper et al. 2010). Initially, the planets migrate towards the convergence zone as was described by LPM10 for individual planets in such a disk. Once the planets are near the convergence zone, however, the close proximity to other planets leads to chaotic interactions and collisions, eventually resulting in the formation of several large bodies that often merge to form a single massive planetary core. The planetary core dominates the dynamics of the remnant bodies, and the smaller bodies tend to get trapped in mean-motion resonances with the core. Some become trapped as Trojans with the core, and the whole system migrates inward on the viscous timescale as the disk evolves, maintaining the resonances. As the goal of this investigation was to study planetary embryos undergoing Type I migration, the simulation does not model accretion onto the planetary core or Type II migration. Both should be treated in future work.

Since the migration torque scales with the mass of the planet, simulations that initially consist of larger mass planetary embryos produce planetary cores rapidly, while simulations that start with less massive bodies often take more than 1 Myr to form a core. The rate of core formation does not appear to depend on the initial distribution of planets in the disk, but does depend on the mass of the planetary embryos that coalesce to form the core. A realistic protoplanetary disk would consist of planetary embryos with a range of masses, but we have shown that even in the case of a Gaussian distribution of embryo masses the trend of large embryos migrating faster and merging earlier holds.

The location of the convergence zone is determined by the temperature profile of the gas disk. This, in turn, is determined by the turbulent viscosity as parameterized by α , the total disk mass, and background illumination from the central star and neighboring stars. The convergence zone falls at larger radii for larger values of α and the disk temperature. More massive stars have hotter disks, leading to convergence zones at larger radii. Direct imaging has indeed revealed a population of giant planets at radii of order 100 AU (e.g. Marois et al. 2008; Kalas et al. 2008; Oppenheimer et al. 2008; Marois et al. 2010) around stars significantly more massive than the Sun. Our results offer a possible means of building gas giant planets via fast core accretion at such large radii.

Partial support for this work comes from NASA grant NNX07AI74G and NSF grant AST10-09802. Some of the computations were performed at the AMNH Parallel Computing Center.

REFERENCES

- Alibert, Y.; Mordasini, C.; & Benz, W. 2004, *A&A*, 417, 25
- Balbus, S. A., & Hawley, J. F. 1991, *ApJ*, 376, 214
- Baruteau, C., Fromang, S., Nelson, R. P., & Masset, F. 2011, *A&A*, 533, A84
- Baruteau, C., & Lin, D. N. C. 2010, *ApJ*, 709, 759
- Baruteau, C., & Masset, F. 2008, *ApJ*, 672, 1054
- Bate, M. R., Lubow, S. H., Oglive, G. I., & Miller, K. A. 2003, *MNRAS*, 341, 213
- Bell, K. R., Cassen, P. M., Klahr, H. H., & Henning, Th. 1997, *ApJ*, 486, 372
- Bitsch, B., & Kley, W. 2011, *A&A*, 530, A41
- Bitsch, B., & Kley, W. 2010, *A&A*, 523, A30
- Birnstiel, T., Dullemond, C. P., & Brauer, F. 2009, *A&A*, 503, L5
- Chambers, J. E., Wetherill, G. W., & Boss, A. P. 1996, *Icarus*, 119, 261
- Cresswell, P., & Nelson, R. P. 2008, *A&A*, 482, 677
- Crida, A., Morbidelli, A., & Masset, F. 2006, *Icarus*, 181, 587
- Cuzzi, J. N., Hogan, R. C., & Bottke, W. F. 2010, *Icarus*, 208, 518
- D'Angelo, G., Henning, T., & Kley, W. 2002, *A&A*, 385, 647
- Davis, S. W., Stone, J. M., & Pessah, M. E. 2010, *ApJ*, 713, 52
- Dohnanyi, J. S. 1969, *J. Geophys. Res.* 74, 2531
- Fleming, T., & Stone, J. M. 2003, *ApJ*, 585, 908
- Hellary, P., & Nelson, R. P. 2012, arXiv:1112.2997 (HN12)
- Hollenbach, D., Johnstone, D., Lizano, S., & Shu, F. 1994, *ApJ*, 428, 654
- Hubeny, I. 1990, *ApJ*, 351, 632
- Kalas, P., Graham, J. R., Chiang, E., Fitzgerald, M. P., Clampin, M., Kite, E. S., Stapelfeldt, K., Marois, C., & Krist, J. 2008, *Science*, 322, 1345
- Kley, W. & Crida, A. 2008, *A&A*, 487, L9
- Kokubo, E. & Ida, S. 1996, *Icarus*, 123, 180
- Laughlin, G., Steinacker, A., & Adams, F. C. 2004, *ApJ*, 608, 489
- Lynden-Bell, D., & Pringle, J. E. 1974, *MNRAS*, 168, 603
- Lyra, W., Paardekooper, S.-J., & Mac Low, M.-M. 2010, *ApJ*, 715, L66 (LPM10)
- Lyra, W., Johansen, A., Klahr, H., & Piskunov, N. 2008, *A&A*, 491, L41
- Marois, C., Zuckerman, B., Konopacky, Q. M., Macintosh, B., & Barman, T. 2010, *Nature*, 468, 1080
- Marois, C., Macintosh, B., Barman, T., Zuckerman, B., Song, I., Patience, J., Lafrenière, D., & Doyon, R. 2008, *Science*, 322, 1348
- Morbidelli, A., Crida, A., Masset, F., & Nelson, R. 2008, *A&A*, 478, 929
- Morbidelli, A., Bottke, W., Nesvorný, D., Levison, H. 2009, *Icarus*, 558, 573
- Movshovitz, N., Bodenheimer, P., Podolak, M., & Lissauer, J. J. 2010, *Icarus*, 209, 616
- Nakamoto, T. & Nakagawa, Y. 1994, *ApJ*, 421, 640
- Nelson, R. P. 2005, *A&A*, 443, 1067
- Nelson, R. P., & Papaloizou, J. C. 2004, *MNRAS*, 350, 849
- Ogihara, M., Ida, S., & Morbidelli, A. 2007, *Icarus*, 188, 522
- Oishi, J. S., & Mac Low, M.-M. 2009, *ApJ*, 704, 1239
- Oppenheimer, B. R., Brenner, D., Hinkley, S., Zimmerman, N., Sivaramakrishnan, A., Soummer, R., Kuhn, J., Graham, J. R., Perrin, M., Lloyd, J. P., Roberts, L. C., Jr., & Harrington, D. M. 2008, *ApJ*, 679, 1574
- Paardekooper, S.-J., Baruteau, C., Crida, A., & Kley, W. 2010, *MNRAS*, 401, 1950
- Paardekooper, S.-J., Baruteau, C., & Kley, W. 2011, *MNRAS*, 410, 293
- Paardekooper, S.-J., & Papaloizou, J. C. B. 2008, *A&A*, 485, 877
- Paardekooper, S.-J., & Papaloizou, J. C. B. 2009, *MNRAS*, 394, 2283
- Paardekooper, S.-J., & Mellema, G. 2006, *A&A*, 459, L17
- Papaloizou, J. C. B., & Terquem, C. 1999, *ApJ*, 521, 823
- Pollack, J. B., Hubickyj, O., Bodenheimer, P., Lisaur, J. J., Podolak, M., & Greenzweig, Y. 1996, *Icarus*, 124, 62
- Rein, H., & Papaloizou, J. C. *A&A*, 497, 595
- Sándor, Zs., Lyra, W., & Dullemond, C. 2011, *ApJ*, 728, L9
- Shakura, N. I., & Sunyaev, R. A. 1973, *A&A*, 24, 337
- Tanaka, H., Takeuchi, T., & Ward, W. R. 2002, *ApJ*, 565, 1257
- Tanaka, H., Inaba, S., & Nakazawa, K. 1996, *Icarus*, 123, 450
- Tanaka, H., Ward, W. R. 2004, *ApJ*, 602, 388
- Uribe, A., Klahr, H., Flock, M., & Henning, Th. 2011, *ApJ*, 736, 85
- Ward, W. R. 1997, *Icarus*, 126, 261
- Yang, C.-C., Mac Low, M.-M., & Menou, K. 2009, *ApJ*, 707, 1233
- Yang, C.-C., Mac Low, M.-M., & Menou, K. 2011, in press (arXiv:1103.3268)